Jiang and Yu *J Infrastruct Preserv Resil* (2023) 4:24
https://doi.org/10.1186/s43065-023-00090-9

Journal of Infrastructure
Preservation and Resilience

RESEARCH

Open Access

Holistic multiphysics simulation of climatic responses of cold region pavements

Yusheng Jiang[1] and Xiong Yu[2*]

Abstract

In cold regions, the environment dynamics lead to variations of soil temperature, water content, and deformation, which are characterized by highly coupled physical interplay. The hydraulic and thermal properties of unsaturated soils are highly nonlinear, which is further complicated when subjected to freezing. This paper presents a comprehensive multiphysics coupling model to evaluate these complex processes. The model considers the behaviors of unsaturated frozen soils. It accounts for the influences of meteorological, geothermal, and hydrological factors. The model is validated through two pavement case studies using Long-Term Pavement Performance (LTPP) road section data. The first case analysis is performed for a pavement section in Vermont, and the simulation lasted for 30 days during a non-freezing season on an hourly basis. The results validated the performance of the model considering unsaturated soil behaviors. The second case study is based on a daily analysis of a pavement section in South Dakota over a freezing–thawing cycle over 194 days. The results validated the model in considering the frozen unsaturated soil behaviors. Both case studies demonstrate the performance of this comprehensive model in quantifying the spatial and temporal variations of soil temperature and water content in response to environmental stressors. The capability of the model in accurately predicting the responses of pavement to the meteorological factors unleashes the potential of this model to assess the effects of climate and climate change on cold region pavement, as well as other types of geo-structures.

Keywords Hydro-thermal coupling, Multiphysics, Cold region, Unsaturated soil, Frozen soil, Climate change

Introduction

The freezing and thawing of soil have long been highlighted as significant contributors to various types of geo-structural failures [1]. From a Multiphysics perspective, the mechanical behavior of soil is closely linked to the changes in temperature and water/ice content, which are driven by environmental factors such as meteorological, hydraulic, and geothermal dynamics. Extensive research has been conducted to investigate the detrimental environmental effects on geo-infrastructure in cold regions, encompassing slope diseases [2–5], the loss of bearing capacity [6–8], damage to embankments [9–11], deterioration of pavements [12–16], and buckling and breakage of pipelines [17–20].

The response of frozen and unfrozen soil to different environmental factors is complex and highly coupled. Numerous of numerical models have been proposed to investigate this intricate process, generally falling into two categories: thermal-hydro (TH) model and thermal-hydro-mechanical (THM) models [21]. While a majority of the TH [22–28] and THM [5, 29–35] have been proven to be effective tools in quantifying the spatial and temporal distribution of temperature and moisture within the soil, few have focused on studying the effects of integrated internal and external environmental loads on

---

*Correspondence:
Xiong Yu
xxy21@case.edu
[1] Department of Civil and Environmental Engineering, Case Western Reserve University, 2104 Adelbert Road, Bingham 203C, Cleveland, OH 44106-7201, USA
[2] Department of Civil and Environmental Engineering, Case Western Reserve University, 2104 Adelbert Road, Bingham 206, Cleveland, OH 44106-7201, USA

geo-structures, like the complex interactions between the atmosphere and frozen soil [3].

Climate factors are widely recognized as significant inducements of geo-structure failures. With the rise of global warming, temperature and precipitation abnormality have led to phenomena such as increased active layer thickness, permafrost degradation, and irregular freeze–thaw cycles, which have been widely observed and reported [36, 37]. Since the end of the last century, plenty of research [8, 13, 14, 38–46] has been conducted to assess the impact of climatic variations on geo-infrastructure in cold region. However, most of these studies give more weight to temperature and rainfall, while the other meteorological parameters (e.g., wind, solar, humidity, and evaporation) are not thoroughly considered. Moreover, the interactions between geo-infrastructure and environment are not only associated with a variety of meteorological factors, but also with geothermal and hydrological forces (e.g., drainage, runoff, ground water, vegetation transpiration, ground heat flux, and moisture or heat source). Figure 1 provides a detailed illustration of soil interactions with the environment, showing the exchange of energy and moisture between the soil and environmental factors. The transfer of energy is represented by red arrows, while the transfer of moisture is represented by blue arrows.

As shown in Fig. 1, the transport of water in soil is driven by both exogenous soil-atmosphere interactions and endogenous hydrological forces. The soil-atmosphere exchanges are contributed by distinct components on the soil surface, and the net water flux can be estimated using the equation [21]:

$$NF = P - E - R - T_r - D \tag{1}$$

where NF is the net water flux in m/s; P is precipitation in m/s; E is the evaporation in m/s; R is the run-off in m/s; T_r is the vegetation transpiration in m/s; and D is drainage in m/s. The endogenous hydrological forces are exerted on domains or boundaries inside of soil, mainly related to drainage, ground water table (GWT) change, and other moisture sources (e.g., pipe leakage and water injection). Similarly, heat alternation in soil is primarily induced by exogenous atmospheric and endogenous geothermal factors on surface and non-surface domains or boundaries. The heat flux balance on the soil-atmosphere surface can be expressed as [47]:

$$Q = Q_s - Q_l + Q_c - Q_e \tag{2}$$

where Q is the net heat flux in W/m^2; Q_s is the shortwave radiation in W/m^2; Q_l is the outgoing longwave radiation in W/m^2; Q_c is the conductive heat flux in W/m^2; Q_e is the evaporation heat flux in W/m^2. The geothermal heat refers to the energy exchanged on the non-surface boundaries or domains of the analyzed soil body. The heat source can originate from chemical reactions, microbial activity, water phase change, adjacent structures (such as thermal piles, wastewater pipes, and electrical cables), and the earth at deep levels or on the sides. Notably, the magnitude of heat from the earth is dependent on the depth of the soil. To be specific, the heat exchange is more active at shallow depths where the thermal gradient is relatively large. Whereas, below a certain depth, the high thermal inertia of the soil often keeps

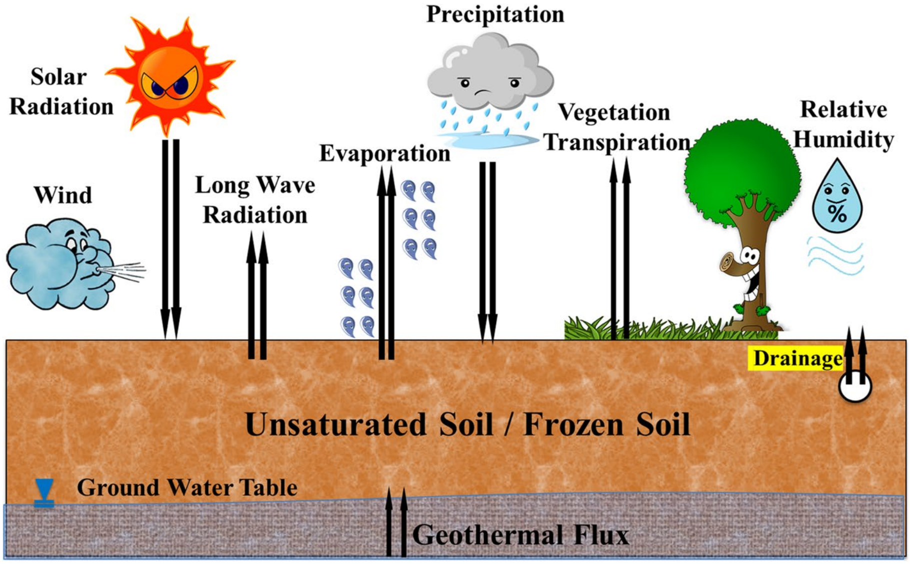

Fig. 1 The sketch of soil interactions with environment

the soil temperature nearly constant, and the heat source from the earth is typically neglected [48].

The current study introduces a comprehensive hydro-thermal model that integrates Fourier's law and a modified form of Richards' equation with formulations of environmental dynamics. This model aims to capture the interactions between the soil and its surroundings, considering meteorological, geothermal, and hydrological factors. By incorporating the energy and mass exchanges between the soil-atmosphere and soil-earth interfaces, the proposed model enables the simulation of geo-infrastructure responses under various environmental effects in cold regions. To solve the highly non-linear partial differential equations of the model, a commercial Finite Element Method (FEM) software, COMSOL Multiphysics 5.5, is employed. In order to validate the proposed model, two case studies on pavement structures are conducted, and the obtained results are compared with field data, which ensures the applicability and reliability of the model predictions.

Theoretical background

Governing equations

The energy conservation in porous media is expressed by a modified Fourier's equation:

$$\mathrm{C_a}\frac{\partial \mathrm{T}}{\partial \mathrm{t}} = \nabla(\lambda\nabla\mathrm{T}) + L_f\rho_i\frac{\partial\theta_i}{\partial t} \tag{3}$$

where $\mathrm{C_a}$ is the volumetric heat capacity in $\mathrm{J/(m^{3\cdot}\ K)}$; T is the temperature in K; t is time; λ is thermal conductivity in $\mathrm{W(m \cdot K)}$; $\mathrm{L_f}$ is latent heat in J/kg; θ_i is the volumetric ice content; ρ_i is the density of ice in $\mathrm{kg/m^3}$. In Eq. (1), the coupling variables $\mathrm{C_a}$ and λ depend upon the proportions of phases (e.g., soil, frozen water, air, and unfrozen water) in the soil. $\mathrm{C_a}$ is estimated by:

$$C_a = C_s\theta_s + C_w\theta_w + C_i\theta_i + C_v(n - \theta_w - \theta_i) \tag{4}$$

where θ represents volumetric content; C represents heat capacity in $\mathrm{J/(m^{3\cdot}\ K)}$; subscripts s, w, i, and v represent soil mass, unfrozen water, frozen water (or ice), and air phase separately. The λ is evaluated by geometric mean method which takes into account the effect of soil particles, liquid water ice, and air on thermal transport [49]:

$$\lambda = \lambda_s^{\theta_s}\lambda_w^{\theta_w}\lambda_i^{\theta_i}\lambda_a^{\theta_a} \tag{5}$$

where λ denotes thermal conductivity and subscripts has same meaning as those of heat capacity in Eq. (4).

The fluid transport in the unsaturated porous media is governed by an extended Richards' equation:

$$\frac{\partial\theta_w}{\partial t} + \frac{\rho_i}{\rho_w}\frac{\partial\theta_i}{\partial t} = \nabla(K_{Lh}\nabla h + K_{Lh}i + K_{LT}\nabla T) \tag{6}$$

where ρ_w represents density of water in $\mathrm{kg/m^3}$; $\mathrm{K_{Lh}}$ is the hydraulic conductivity associated with pore pressure head in m/s; $\mathrm{K_{LT}}$ is the hydraulic conductivity caused by temperature gradient in m/s; h is the matric suction in m (water pressure unit); i is the unit vector of the gravity direction.

The Van Genuchten's equations [50] of soil–water characteristics curve (SWCC) is used to describe the relationship between suction and unfrozen water content for either unfrozen and frozen soil [51]. In addition, the hydraulic conductivity in Eq. (6) is evaluated by Van Genuchten's equations via [22]:

$$S_e = \frac{\theta - \theta_r}{\theta_s - \theta_r} = \left(1 + |\alpha h|^n\right)^{-m} \tag{7}$$

$$K_{Lh} = K_sS_e^l[1 - \left(1 - S_e^{\frac{1}{m}}\right)^m] \tag{8}$$

$$K_{LT} = K_{Lh}(\frac{hG_{wT}}{\gamma_0}\frac{d\gamma}{dT}) \tag{9}$$

$$K_{fLh} = 10^{-\Omega Q}K_{Lh} \tag{10}$$

where $\mathrm{S_e}$ denotes the effective saturation; θ_s and θ_r are the saturated and residual water content in percentage separately; α, m, n, and l are material-specified constants determined by SWCC curve; K_s is the saturated hydraulic conductivity in m/s; γ is the surface tension of soil water in gs^2, which depends on temperature and is evaluated as $\gamma = 75.6 - 0.145\mathrm{T} - 2.38 \times 10^{-4}T^2$(T is in degC); K_{fLh} is the hydraulic conductivity associated with pore pressure head of frozen soil in m/s, which considers the impedance impact of ice on moisture migration; Ω is impedance factor related to material type; and Q is the ratio of θ_i to $\theta_i + \theta_s - \theta_r$. The volumetric ice content in Eq. (6) is evaluated by empirical equations [52, 53]

$$B(T) = \frac{\theta_i}{\theta_w} = \begin{cases} \frac{\rho_w}{\rho_i}\left(\left|\frac{T}{T_f}\right|^b - 1\right)\left(T < T_f\right) \\ 0\left(T \geq T_f\right) \end{cases} \tag{11}$$

$$\theta_i = B(T) * \theta_w \tag{12}$$

where B is the volumetric content ratio of ice and unfrozen water content; T is the temperature in K; T_f is the freezing point in K; b is the empirical coefficients associated with the soil type (0.56 for clay, 0.47 for silt, and 0.61 for sand and gravel).

Environmental factors

The proposed model integrates various environmental effects through boundary condition equations. For the thermal field, effects of solar short-wave radiation, upward longwave radiation, heat convection, ground heat flux are considered by Neumann boundary conditions. Meanwhile, for the hydraulic field, the model incorporates the influence of precipitation, groundwater elevation change, and drainage using either Neumann or Dirichlet boundary conditions.

In the thermal field, the absorption of short waver radiation on the soil surface can be described by [54]:

$$q_s = (1 - albedo) * S \tag{13}$$

where q_s is the short-wave absorption of the solar radiation; the albedo is the solar reflectivity; S is the solar radiation in $(\mathrm{W/m^2})$. The total long wave radiation (including outgoing radiation and counter-radiation) on the structure surface follows the Stefan-Boltzmann law and is described as [55]:

$$q_l = \epsilon\sigma T_s^4 - \epsilon_a \sigma T_{sky}^4 \tag{14}$$

$$T_{sky} = \left(0.754 + 0.0044 T_{dp}\right)^{0.25} * T_{amb} \tag{15}$$

$$T_{dp} = T_{amb} - \frac{100 - RH}{5} \tag{16}$$

where total q_l is the long-wave radiation; ϵ is the emission coefficient; ϵ_a is the absorption coefficient of pavement; here the assumption is $\epsilon = \epsilon_a$ to simplify the analysis; σ is the Stefan–Boltzman constant equals to $5.68 * 10^{-8} W * m^{-2} * K^{-4}$; T_s is the pavement surface temperature in K; T_{sky} is the effective ambient temperature above the structure in K; T_{dp} is the dewpoint temperature in K which is the temperature needed to cool and make the air saturated; RH is relative humidity in percentage. T_{amb} is the ambient air temperature in K. In addition to by Eq. (15), the effect of ambient air temperature is also reflected by convective heat flux on structure surface through Newton's law of cooling [56]:

$$n \cdot (\lambda \nabla T) = h_c (T_{amb} - T) \tag{17}$$

$$h_c = \begin{cases} 5.6 + 4 * v_{wind}\, for\ v_{wind} \le 5m/s \\ 7.2 + 4 * v_{wind}^{0.78}\, for\ v_{wind} > 5m/s \end{cases} \tag{18}$$

where n is the normal unit vector of the boundary ; λ_c is the thermal conductivity in $\mathrm{W/(m \cdot K)}$, T is the temperature at boundaries in K; and $\mathrm{h_c}$ is the convection heat transfer parameter in $\mathrm{W/(m^{2\cdot}\ K)}$. As shown in Eq. (17) and 18, not only the ambient air temperature but also the wind speed together with soil surface temperature worked concurrently to determine the convective heat exchange. The geothermal effect by surrounding earth is calculated by:

$$q_g = \lambda_{botom} \nabla T_{bottom} \tag{19}$$

where λ_{botom} and ∇T_{bottom} are the thermal conductivity in $\mathrm{W/(m \cdot K)}$ and temperature gradient in K/m of the material on the non-surface boundaries of the analyzed soil domain. The heat source other than geothermal earth heat is not incorporated into the current model.

In the hydraulic field, the extended Horton empirical equation [57] is used to evaluate the infiltration rate by:

$$I = \begin{cases} RI\ for\ RI < RC \\ RC\ for\ RI > RC \end{cases} \tag{20}$$

$$RC = i_f + (i_0 - i_f)\exp[-\left(\frac{RI}{i_f}\right)\left(\frac{K_s}{i_f}\right)^{0.5} t] \tag{21}$$

where I is infiltration rate in mm/s; the RI is the rainfall intensity in mm/s; RC is the infiltration capacity in mm/s; i_0 is initial infiltration capacity;i_f is the final infiltration capacity; K_s is the saturated hydraulic conductivity in m/s. i_0 can be associated with in-situ suction and i_f are usually assumed to be equal or smaller than the K_s. The GWT is normally located at the interface where the positive and negative pore water pressure is separated with zero water pressure on. The position of GWT can indicate water pressure along vertical direction of the soil. When the GWT is higher than the bottom boundary, the positive saturated pore water pressure is exerted on it. Whereas, when the GWT is lower than the bottom boundary, the negative suction pressure under static condition (moisture movement balance between gravity and suction gradient) is applied on it. In the proposed model, either Dirichlet boundary condition or Neumann boundary condition can be added on the lower boundary condition to reflect the groundwater effect.

Verication by case study

The coupled model with integrated environmental force expressions shows considerable nonlinearity, posing a challenge for solution. To address this, the software COMSOL Multiphysics 5.5 with an advanced solver is employed in this study to numerically solve the model equations. Two separate scenarios of pavement in cold regions are analyzed. The first case is an hourly-based 1-D analysis spanning one month during a non-freezing season, which aims to validate the performance of the model under non-freezing conditions and demonstrates its sensitivity to environmental inputs of relatively small time scale. The second case entails a 2-D analysis conducted on a daily basis, extending over more than half a year. The aim is to test the applicability of the model in simulating the response of geo-infrastructures to environmental loads of cold regions. The parameters utilized in the simulation are found from literature [21, 58] or through calibration, as detailed in Tables 1, 2 and 3. Since the pavement surface material is asphalt concrete, a material with very low permeability, only thermal field calculations are conducted for this layer, while moisture transfer is not considered during the simulation. However, for the layers beneath the asphalt (base and subgrade layer), both thermal and hydraulic processes are evaluated.

The COMSOL software incorporates robust and versatile solvers capable of handling strong nonlinearities inherent in governing equations. Given this capability, COMSOL was chosen to address the model under study, characterized by significant nonlinearity. While COMSOL provides a fixed time step option, it also offers an adaptive time-stepping mechanism. This feature dynamically adjusts the time step size based on a predefined tolerance, enhancing stability, accuracy, computational efficiency, and convergence, especially in complex nonlinear simulations. To enhance model convergence, the adaptive time step was employed for both cases. Additionally, specific solver settings within COMSOL were adjusted. The absolute tolerance was set using the global method and scaled to a factor of 1e-5. Within the fully coupled solver, the non-linear approach was designated as “Automatic (Newton),” with maximum number of more than four iterations. Mesh sizes for the two cases were determined by mesh refinement studies. The built-in mesh setting labeled “Extra fine (pre-defined)” was found to strike a balance between computational efficiency and error stabilization, and was thus applied to both cases.

Table 1 The common simulation parameters for the two cases

Symbol	value (unit)	Description
λ_s	1.9[W/(m*K)]	Thermal conductivity of soil solid
λ_w	0.58[W/(m*K)]	Thermal conductivity of soil water
λ_i	2.23[W/(m*K)]	Thermal conductivity of soil ice
λ_a	0.025[W/(m*K)]	Thermal conductivity of soil air
C_n	2e6[J/(m^3*K)]	Volumetric heat capacity of Solid
C_w	4.2e6[J/(m^3*K)]	Volumetric heat capacity of Liquid
C_v	1.2e3[J/(m^3*K)]	Volumetric heat capacity of Vapor
C_i	1.935e6[J/(m^3*K)]	Volumetric heat capacity of Ice
L_f	3.34e5[J/kg]	Latent heat of freezing
L_0	3.34e8[J/m^3]	Volumetric Latent heat of freezing
γ_0	71.89[g*s^-2]	Surface tension of soil water at 25 Celsius degrees
ρ_i	931[kg/m^3]	Density of ice
ρ_w	1000[kg/m^3]	Density of water
ρ_n	2700[kg/m^3]	Density of soil solids
g	9.8[m*s^-2]	Gravitational acceleration
ϵ	0.95	Emission coefficient of pavement surface material
ϵ_a	0.95	Absorption coefficient of pavement surface material

Table 2 The simulation used parameters for Case 1

Symbol	value (unit)	Description
K_{s1}	6e-2[m/s]	Saturated hydraulic conductivity of base
K_{s2}	9e-3[m/s]	Saturated hydraulic conductivity of subgrade
θ_{s1}	0.35	Saturated volumetric water content of base
θ_{s2}	0.43	Saturated volumetric water content of subgrade
θ_{r1}	0.075	Residual volumetric water content of base
θ_{r2}	0.015	Residual volumetric water content of subgrade
α_1	1.817	Van Genuchten model coefficient of base
α_2	0.183	Van Genuchten model coefficient of subgrade
l_1	0.5	Van Genuchten model coefficient of base
l_2	0.5	Van Genuchten model coefficient of subgrade
m_1	0.392	Van Genuchten model coefficient of base
m_2	0.240	Van Genuchten model coefficient of subgrade
n_1	1.645	Van Genuchten model coefficient of base
n_2	1.316	Van Genuchten model coefficient of subgrade
Ω_1	7	Van Genuchten model coefficient of base
Ω_2	7	Van Genuchten model coefficient of subgrade
C_{pp}	2e6[J/(m^3*K)]	Heat capacity of pavement surface material
λ_p	1.9[W/(m*K)]	Heat conductivity of pavement surface material
albedo	0.3	Solar reflectivity
ϵ	0.93	Emission coefficient of pavement surface material
ϵ_a	0.93	Absorption coefficient of pavement surface material

Case 1: hourly -based non-freezing season simulation

Case 1 analysis is conducted using data from the LTPP Sect. 50–1002. This site is situated in Vermont

Table 3 The parameters used for simulation Case 2

Symbol	value (unit)	Description
K_{s1}	1.3e-3[m/s]	Saturated hydraulic conductivity of base
K_{s2}	1e-6[m/s]	Saturated hydraulic conductivity of subgrade
θ_{s1}	0.27	Saturated volumetric water content of base
θ_{s2}	0.43	Saturated volumetric water content of subgrade
θ_{r1}	0.08	Residual volumetric water content of base
θ_{r2}	0.06	Residual volumetric water content of subgrade
α_1	0.028	Van Genuchten model coefficient of base
α_2	0.020	Van Genuchten model coefficient of subgrade
l_1	1	Van Genuchten model coefficient of base
l_2	1	Van Genuchten model coefficient of subgrade
m_1	0.614	Van Genuchten model coefficient of base
m_2	0.137	Van Genuchten model coefficient of subgrade
n_1	2.587	Van Genuchten model coefficient of base
n_2	1.196	Van Genuchten model coefficient of subgrade
Ω_1	2	Van Genuchten model coefficient of base
Ω_2	0.5	Van Genuchten model coefficient of subgrade
b_1	0.6	Ice content coefficient of base
b_2	0.5	Ice content coefficient of subgrade
C_{pp}	2.314e6[J/(m^3*K)]	Heat capacity of pavement surface material
λ_p	1.1[W/(m*K)]	Heat conductivity of pavement surface material
albedo	0.22	Solar reflectivity
ϵ	0.95	Emission coefficient of pavement surface material
ϵ_a	0.95	Absorption coefficient of pavement surface material

(44°07′10.6"N 73°10′45.8"W). The pavement layer information is summarized in Table 4. Parameters utilized for each layer in the simulation are presented in Table 2.

At this site, hourly-monitored meteorological, subsurface temperature, and subsurface moisture content data are collected from the LTPP database. The data are employed for the 1-D case analysis with an hourly time scale. The simulation starts from 05/02/2001 6:00am and ends at 05/31/2001 6:00 am. Initial conditions for the simulation are based on MRC Thermistor and TDR measurements of temperature and moisture content from the simulation start date. The effects of environmental factors, such as air temperature, precipitation, solar short-wave radiation, wind speed, relative humidity, geothermal temperature gradient, and ground water table elevation, are considered through corresponding boundary conditions. Figure 2 shows the temporal fluctuations in air temperature, precipitation, solar short-wave radiation, wind speed, relative humidity, and geothermal temperature gradient over the simulation period. On the lower point boundary of the model at 2m depth, as shown in Fig. 2 (c), the temperature gradient is calculated based on the site-measured temperature above and below this depth and is then used to estimate the time-series geothermal flux following Eq. (19). To simulate the soil-atmosphere energy exchange process, the heat flux induced by solar short-wave radiation, long wave radiation, and air convection are applied to the top point boundaries of the 1-D model. Geothermal heat flux is added to the bottom point boundary to simulate geothermal energy migration. The GWT is around 1.1m below the pavement surface and remained constant during the

Table 4 The pavement layer information for Case 1

Layer #	Material	Thickness (m)
3	Asphalt concrete: Hot Mixed, Hot Laid AC, Dense Graded	0.216
2	Unbound (granular) base: Crushed Gravel	0.650
1	Subgrade (untreated): Coarse-Grained: Poorly Graded Gravel with Silt and Sand	1.134

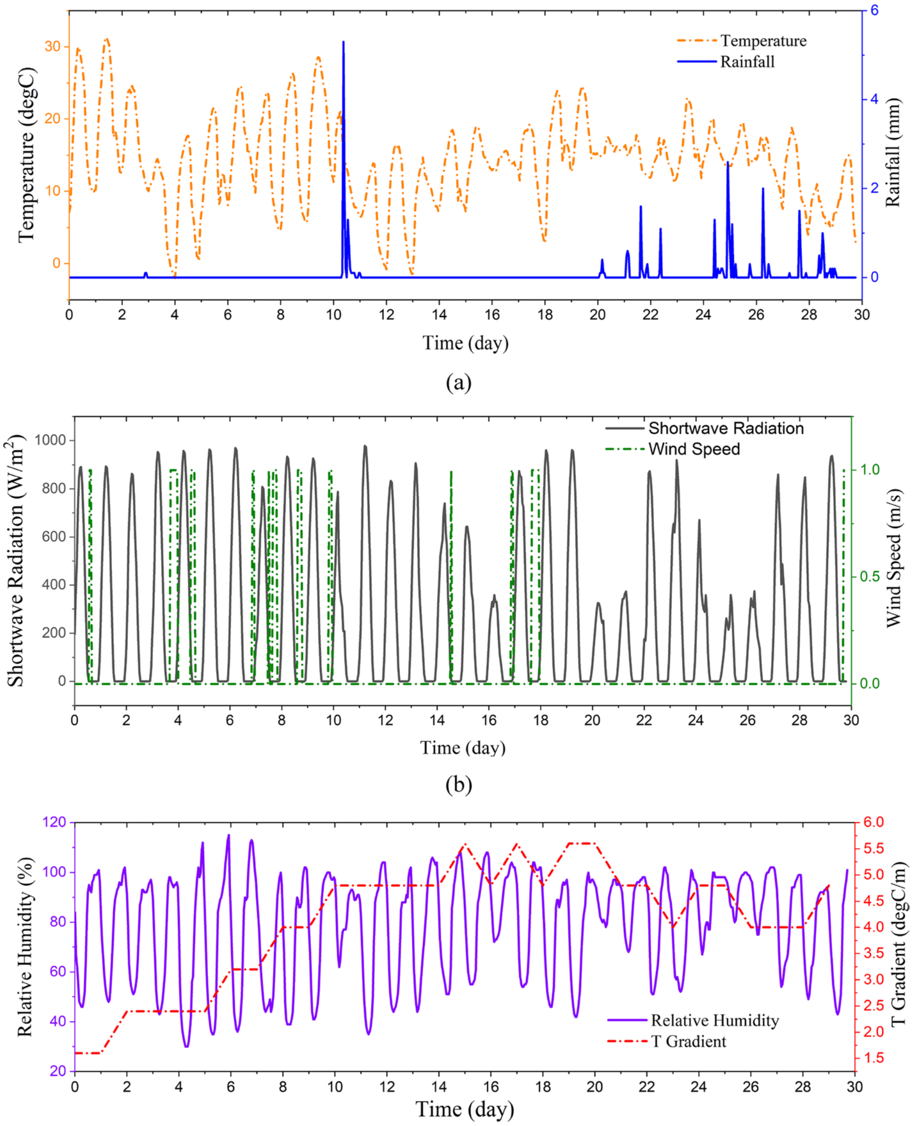

(a)

(b)

(c)

Fig. 2 Environmental factors variation with time from 05/02/2001 to 05/31/2001: **a** temperature and rainfall; **b** Solar shortwave radiation and wind speed; **c** relative humidity and geothermal related temperature gradient

simulation. The precipitation-induced water flux and ground water-related Dirichlet boundary (constant positive water pressure) are added to the top and bottom point boundaries, respectively, to simulate water transfer driven by environmental forces.

It's interesting to note that the meteorological data are likely correlated with each other. For example, the amplitude of temperature fluctuation decreases when precipitation is present, as illustrated in Fig. 2 (a). Furthermore, on rainy days, the wind speed tends to have low value, as shown in Fig. 2 (b), and the daily relative humidity fluctuation range also exhibits a reduction. Shortwave radiation, ambient temperature, and relative humidity display daily periodic variation trends. The peaks of radiation, temperature, and relative humidity usually occurred in noon, afternoon, and after midnight, respectively, with corresponding troughs transpiring approximately 12 h later. The increase or decrease in radiation crest usually follows a consistent, albeit time-lagged, increase or decrease of the temperature crest. After accounting for the time lags, a positive correlation between radiation and temperature becomes evident. These observations implies that there is greater energy influx into the soil from atmosphere during daytime compared to nighttime.

The model estimated results are presented and compared with the site measured data in Figs. 3 and 4. Overall, the simulated temperature aligns well with the site data. In Fig. 3, the temperature fluctuated periodically in both asphalt concrete layer (near surface) and the base layer (in the middle of the layer). It is believed that these periodic temperature trends stem from the cyclic heat exchange of radiation (both shortwave ingoing and longwave outgoing) and convection. The timing of the simulated temperature peak and troughs matches perfectly with the site data in in Fig. 3, indicating the sufficient model sensitivity and adaptability to respond to rapidly changing energy dynamics. The LTPP database does not provide hourly-monitored temperatures below 0.8m but does offer daily average temperature profiles at greater depths. To assess the performance of the model in deeper soil, the simulated temperature profile on day 15(a midpoint of the simulation) and day 28 (near the end of the simulation) are plotted and compared with the LTPP site data in Fig. 4. As shown in Fig. 4, the temperature profile predictions generally align with those of the actual site, demonstrating the capability of the model to predict temperatures at various depths after considering complex environmental inputs.

The hydraulic field comparison results are displayed in Fig. 5. Coherent water content variation trends are observed between the predictions and site measurements for the two examined depths. As shown in Fig. 5,

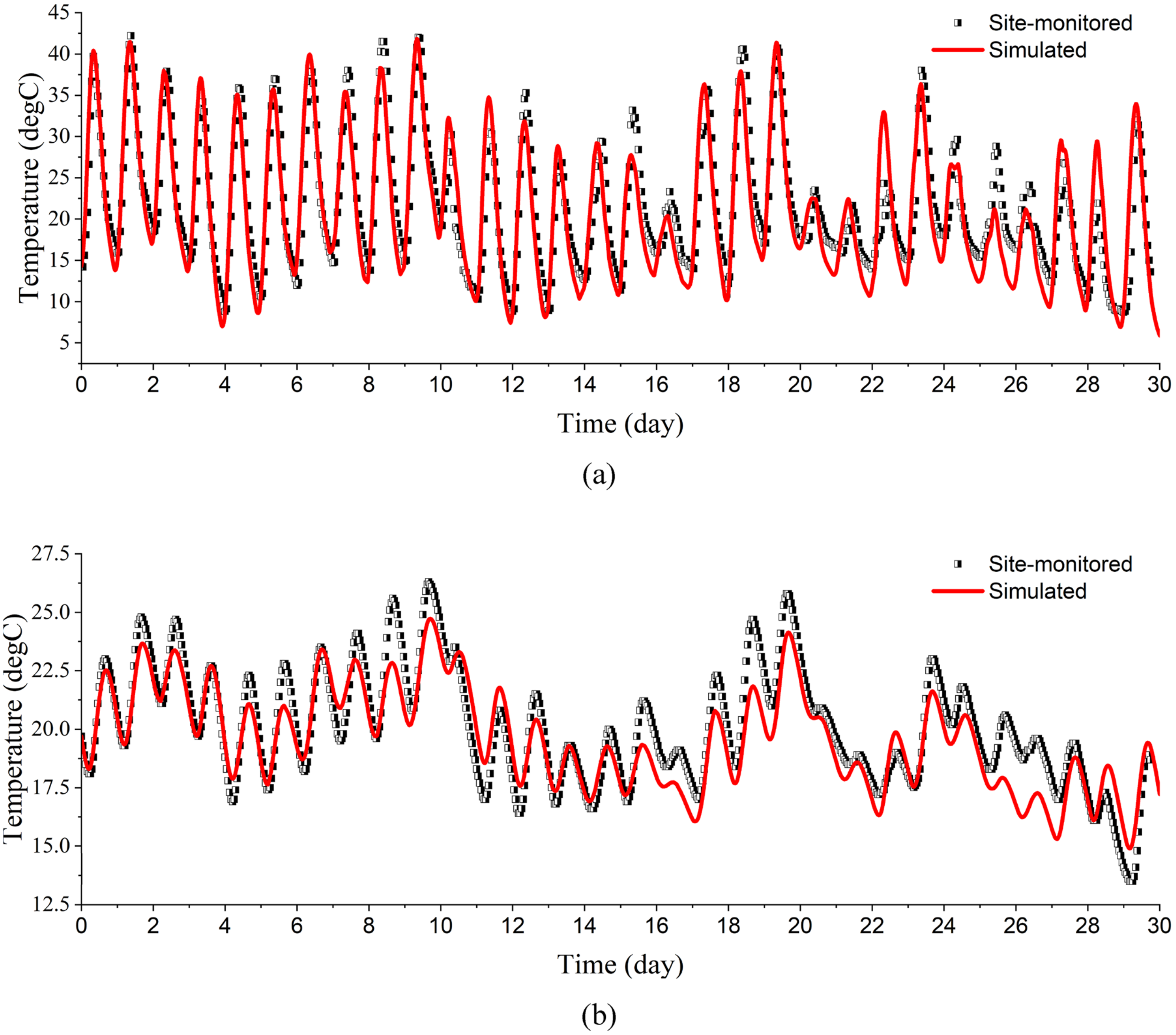

Fig. 3 The comparison between simulation and site measurement: **a** temperature at 0.03 m depth in asphalt layer; **b** temperature at 0.68 m depth in base layer

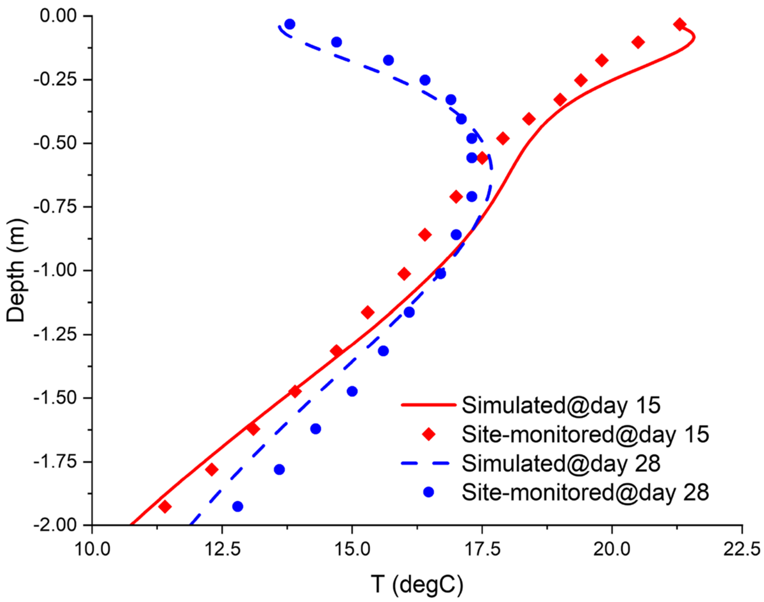

Fig. 4 The simulated temperature profiles on day 15 (a middle time of the simulation) and on day 28 (a nearly end time of the simulation) vs. the site monitored temperature profiles

the moisture content remains nearly constant before day 10. The surge of water content after day 10 is very likely induced by rainfall as shown in Fig. 2(a).The water drains following the day 10 surge, resulting in declining water content before day 20. After the day 20, the water content fluctuated due to a series of precipitation in the following days. The timing of the simulated moisture content peaks basically aligns with the site data, demonstrating the model's ability to effectively capture the water flux disturbances caused by rainfall. Due to the lack of detailed soil data, the simulation assumed homogeneous base layer with consistent parameters. The slightly underestimated water content in Fig. 5 (a) after day 10 may be attributed to uneven hydraulic properties at the actual site. Another possible reason for the underestimated water content after day 10 could be that the model does not incorporate vapor condensation and evaporation processes.

Case 2: daily based seasonal simulation

The analysis for Case 2 employed data from the LTPP Sect. 46–0804 in South Dakota (45°55′40.7"N 100°24′31.7"W). In Case 2, daily monitored data are used for a 2-D and daily-time-scale analysis. The pavement geometry is shown in Fig. 6 and consists of a three-layer system with a 1:3 slope ratio. The detailed layer information is summered in Table 5. It is assumed the pavement system is symmetric, and only the right-hand side of the pavement is modeled.

An analysis spanning 194 days is conducted, starting from 09/01/2020 and ending on 03/15/ 2021. Initial conditions for the simulation are determined using average daily temperature and moisture content data measured by MRC Thermistor and TDR on the simulation start date. Similar as Case 1, boundary conditions for distinct environmental factors are incorporated in Case 2, from which the effects of air temperature, precipitation, solar short-wave radiation, wind speed, relative humidity, geothermal temperature gradient, and groundwater table elevation are evaluated. Figure 7 displays the variation of these environmental factors over time. To simulate the energy exchange between pavement surface and atmosphere, flux by short-wave radiation, long wave radiation, air convection, and precipitation, are applied to the upper three boundaries (boundary 1 to 3 as shown in Fig. 6). In Fig. 7 (c), the temperature gradient on lower boundary is evaluated using the site-measured temperature near the 2m depth, by which the geothermal flux variation with time is calculated. Geothermal effects are then simulated by setting Neumann boundary with this flux on boundary 7. Given the relatively low rainfall intensity and relatively high soil saturated permeability, it is assumed the rainfall intensity is always lower than the infiltration capacity, so the precipitation induced water flux equals to the rainfall intensity. The precipitation boundary is applied on boundary 5, 6 and 3 in Fig. 6. The GWT data for the site are unavailable, so the GWT is assumed to be located 1.25m below the pavement surface at the beginning of the simulation. The GWT level changes to 2m on day 75 and to 2.5m on day 200, and the effect of GWT is simulated using a Dirichlet boundary with linearly

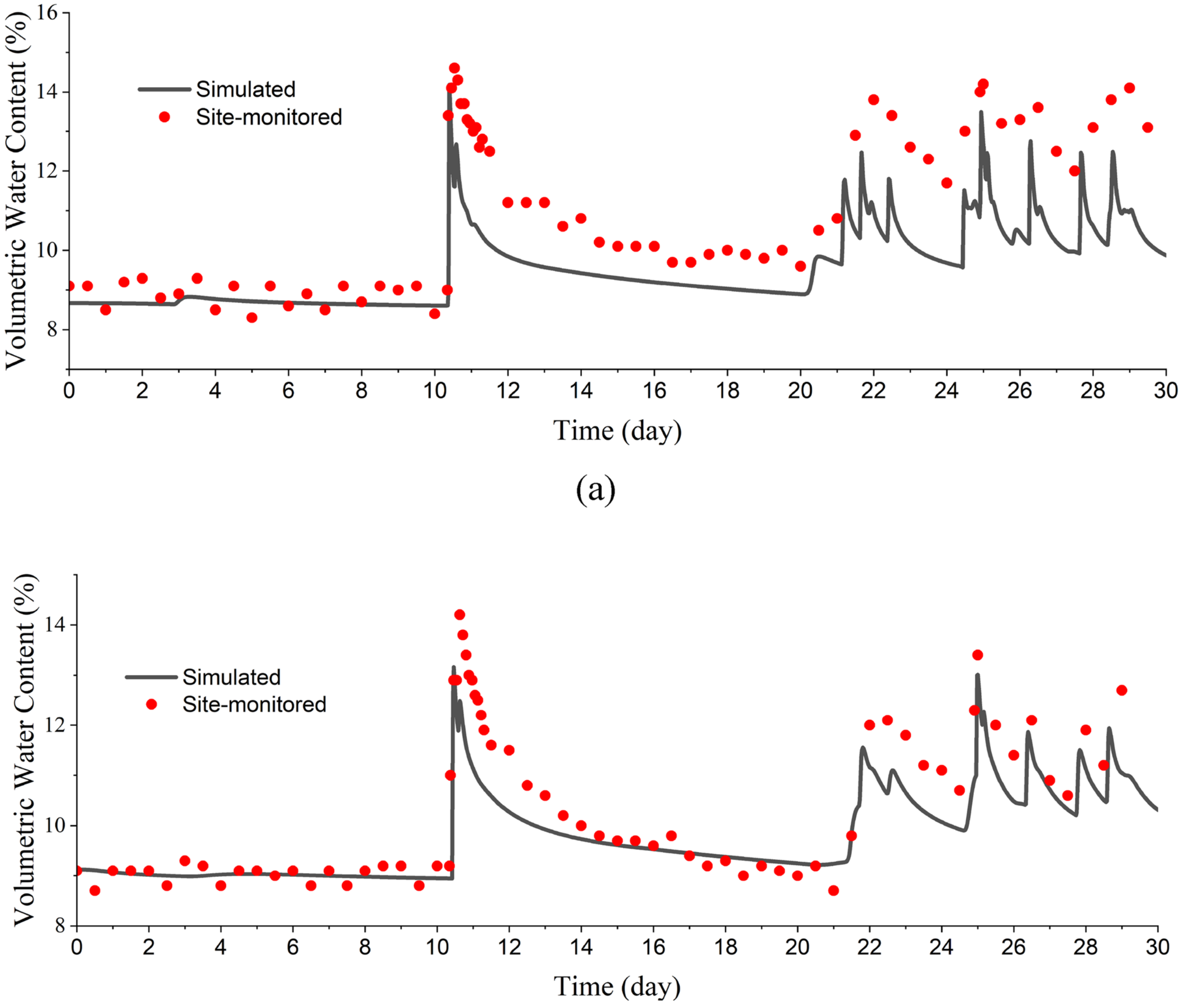

(a)

(b)

Fig. 5 The comparison between simulation and site measurement: **a** volumetric water content at 0.37 m depth in shallow base layer; **b** volumetric water content at 0.66 m depth in deeper base layer

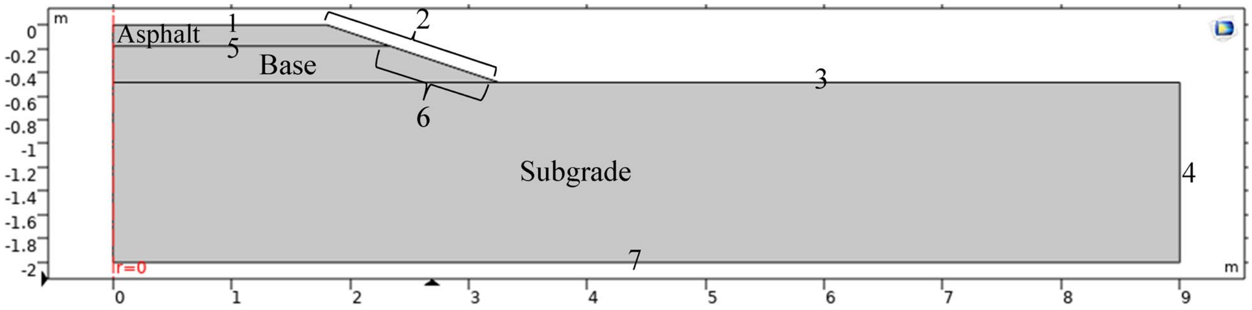

Fig. 6 The geometry of the three-layer pavement system for case 2

Table 5 The pavement layer information for case 2

Layer #	Material	Thickness (m)
3	Asphalt concrete: Hot Mixed, Hot Laid AC, Dense Graded	0.180
2	Unbound (granular) base: Crushed Stone	0.305
1	Subgrade (untreated): Silt and silty sand	1.515

changing pressure head applied to boundary 7. The right boundary 4 in Fig. 6 is assumed to be thermal insulated and hydraulic insulated.

The water content, temperature, and frost depth variation with depth together with time are calculated by the coupling model. The simulation results are compared with site-monitored daily ground temperature and daily moisture of the Sect. 46–0804. Figure 8 compares the measured and simulated temperature variations at different depth (with burried MRC Thermistor) along the pavement axis of symmetry (The left side boundary in Fig. 6). The selected MRC Thermistor burry depth are

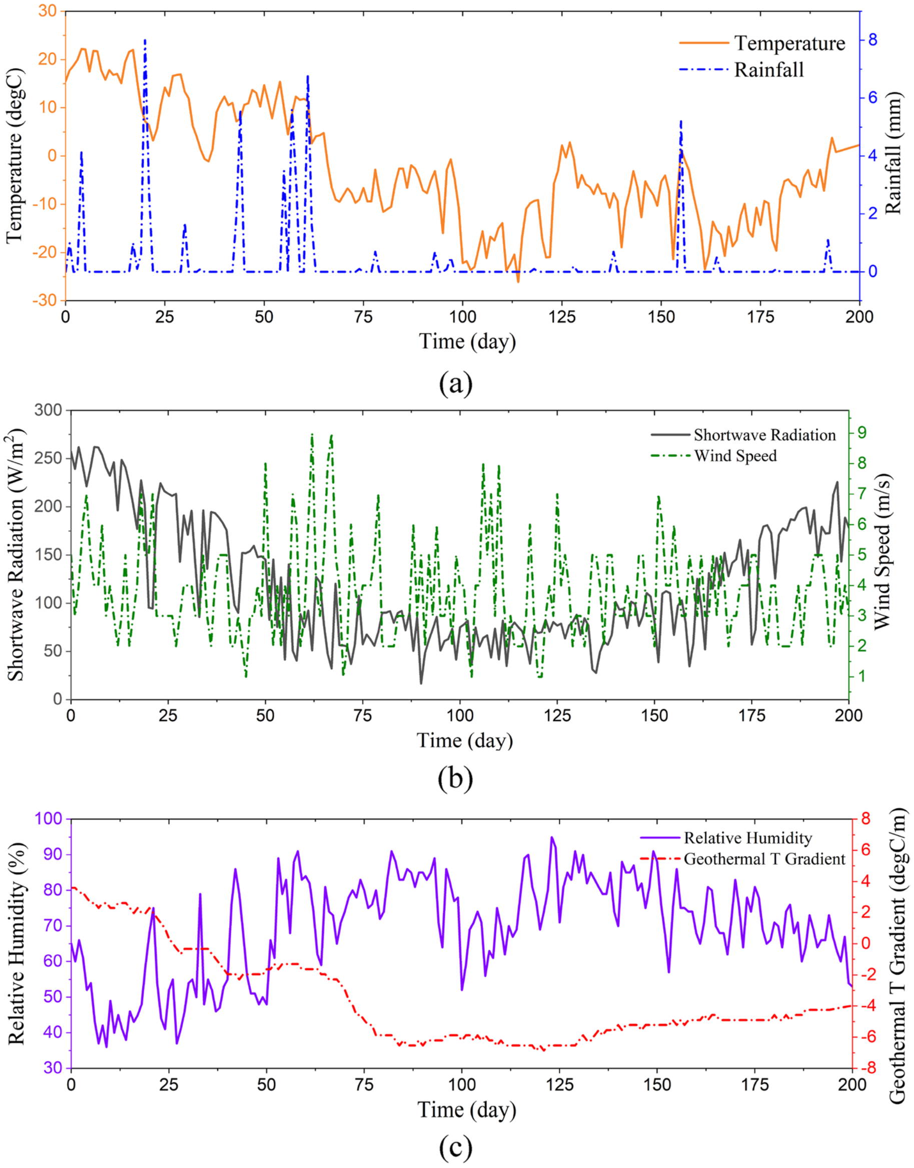

Fig. 7 Environmental factor variations with time from 09–01-2000 to 03–15-2021: **a** temperature and rainfall; **b** solar shortwave radiation and wind speed; **c** relative humidity and geothermal related temperature gradient

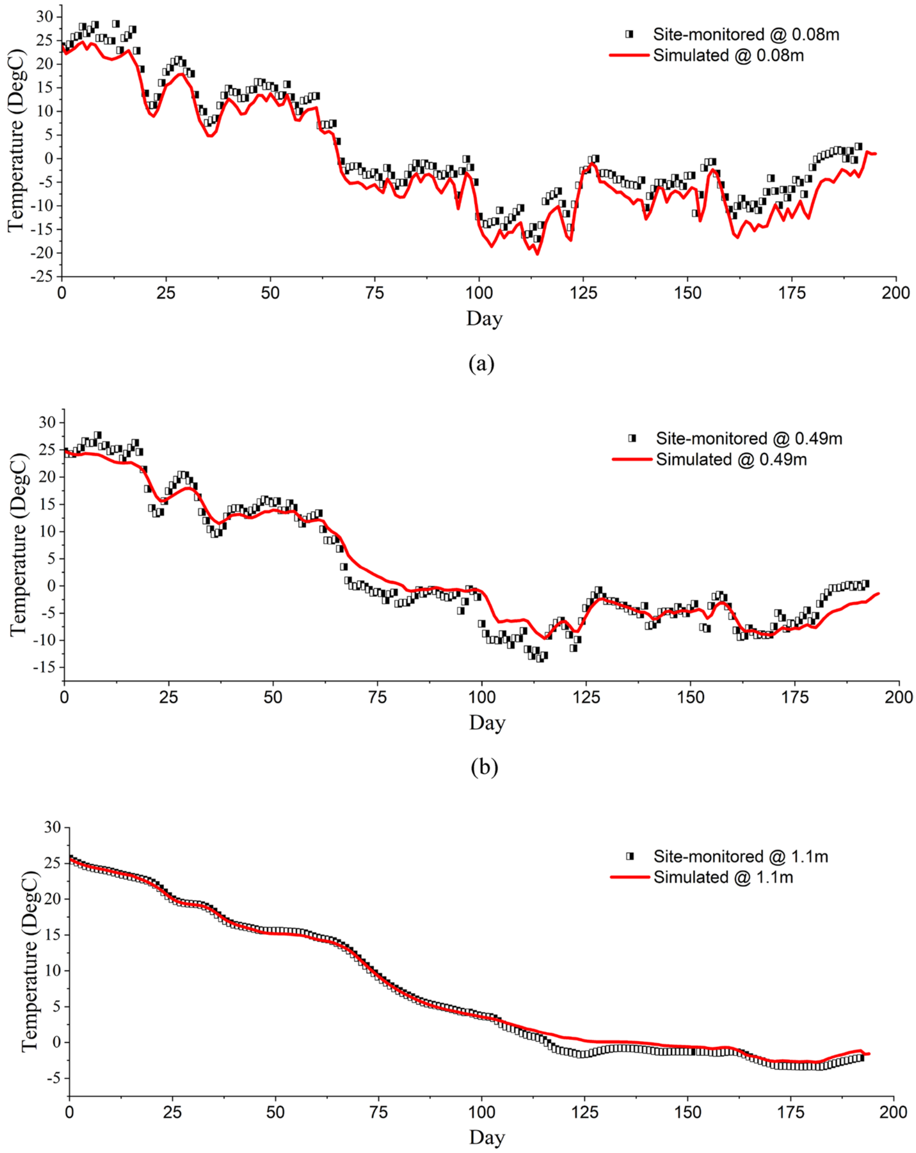

(a)

(b)

(c)

Fig. 8 Simulated and measured temperatures versus time: **a** at 0.08 m in asphalt layer; **b** at 0.49 m in base layer; **c** at 1.1 m in subgrade layer (along pavement axis of symmetry)

0.08 m in asphalt layer, 0.49 m in base layer, and 1.1 m in subgrade layer below pavement surface. Similarly, the measured and simulated unfrozen moisture content variations at different TDR depth (0.33 m in base layer, and 1.1 m in subgrade layer) are compare in Fig. 9. The comparison between simulated and field measured frost depth with time is shown in Fig. 10. As seen from Figs. 8, 9 and 10, the simulation results well match the site measured values at the selected depth, temporally and spatially. This validates the performance of the model to capture the thermal as well as hydraulic filed response of soil to environmental factors during the non-freezing state, freezing state, and the transition process from non-freezing to freezing state.

According to the observations in Fig. 9, both the simulated and site-monitored water content at a depth of 0.33 m exhibited fluctuations prior to day 70, which are likely induced by precipitation, as all water content crests occurred sooner after rainfall (see Fig. 7). After day 70, the water content sharply declined. Since TDR can only measure unfrozen water content, not the total water content, such abrupt decrement is explained as

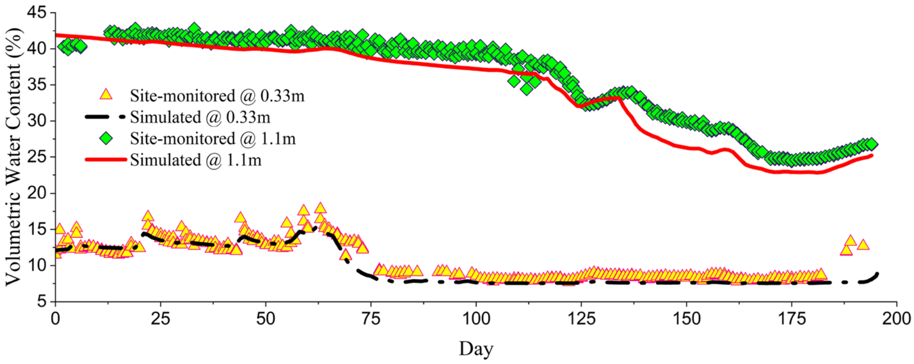

Fig. 9 Simulated and measured unfrozen volumetric moisture content versus time at 0.33 m in base layer and 1.1 m in subgrade layer (along pavement axis of symmetry)

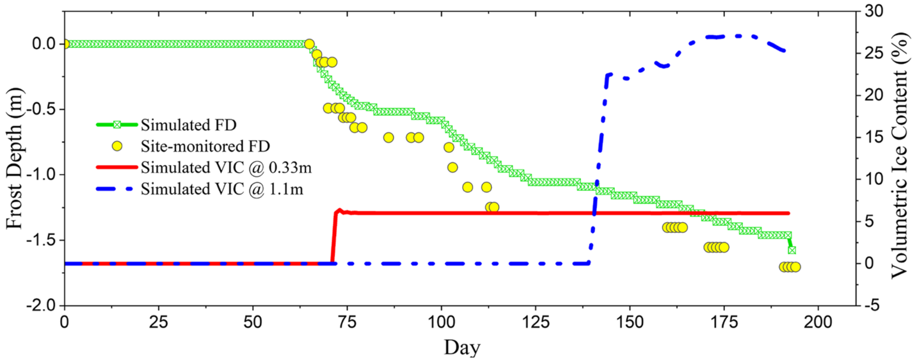

Fig. 10 Frost depth and volumetric ice content (along pavement axis of symmetry) versus time

the conversion of unfrozen water to ice under low temperature. Conversely, at a depth of 1.1 m, the water content slightly decreased from day 1 until approximately day 137, which is likely the results of the dropped GWT. After day 137, the water content exhibited a more pronounced decrease, which is also illustrated as the results of soil freezing.

Figure 10 depicts the temporal variations in volumetric ice content (VIC) at depths of 0.33 and 1.1 m, along with a comparison between the site-measured frost depth (FD) and the simulated FD. The comparison reveals a generally consistent but a slightly underestimated FD. Moreover, a comparison of the results presented in Figs. 9 and 10 indicates that the timing of the sudden decrease in unfrozen water content at depths of 0.33 and 1.1 m coincides with the timing of FD penetrating to these depths and the initiation of the increase in VIC at these depths. These observations proves that the primary cause of the noticeable decline in unfrozen water content, as presented in Fig. 9, is the freezing of the soil. The results presented in Fig. 10 effectively showcase the ability of the model to estimate the timing of ice formation and evaluate the temporal evolution of FD under the environmental dynamics of cold region.

Conclusions

In this study, a comprehensive coupling model was developed to assess the response of geo-infrastructure to different environmental dynamics. Two case analyses were conducted to evaluate the model's performance under different conditions, including geometry dimensions (1D and 2D), input time scale (hourly and daily), simulation durations (1 month and more than half a year), and seasons (non-freezing and transition from non-freezing to freezing). In Case 1, the model demonstrated its commendable sensitivity and adaptability in handling rapidly changing heat inputs. The predicted temperatures at different depths aligned well with the observed data, and the variation trend of water content was generally captured. In Case 2, the model performance was evaluated during the non-freezing, freezing, and transition stages. The model effectively simulated the thermal and hydraulic reactions of the pavement structure to environmental factors under different stages. The two case analyses highlight the potential of the model to provide valuable insights into evaluating the effects of environmental factors on geo-infrastructures in cold regions. The model shows promise in providing recommendations for design adaptations in response to climate change, predicting environmental geohazards, and addressing engineering concerns with geo-infrastructure in cold regions.

Authors' contributions
Xiong (Bill) Yu: envision the study, secure funding, guide study process, discuss the results. Yusheng Jiang: develop model and analyses. All authors reviewed the manuscript.

Funding
This research is partially supported by the National Cooperative Highway Research Program (NCHRP) and US DOT National University Transportation Center.

Availability of data and materials
The data and code are available upon request.

Declarations

Ethics approval and consent to participate
No human subject or animals are involved in the study.

Consent for publication
The authors consent the publications of this paper.

Competing interests
The authors declare no competing interests.

Received: 13 July 2023 Revised: 22 September 2023 Accepted: 25 September 2023

References

1. Gens A (2010) Soil-environment interactions in geotechnical engineering. Geotechnique 60(1):3–74. https://doi.org/10.1680/geot.9.P.109
2. Ishikawa T, Tokoro T, Seiichi M (2015) Geohazard at volcanic soil slope in cold regions and its influencing factors. Jpn Geotech Soc Spec Publ 1(1):1–20. https://doi.org/10.3208/jgssp.key-1
3. Jiang H, Liu Q, Wang Z, Gong J, Li L (2022) Frost heave modelling of the sunny-shady slope effect with moisture-heat-mechanical coupling considering solar radiation. Sol Energy 233(23):292–308. https://doi.org/10.1016/j.solener.2022.01.040
4. Li J, Zhou K, Liu W, Zhang Y (2018) Analysis of the effect of freeze–thaw cycles on the degradation of mechanical parameters and slope stability. Bull Eng Geol Env 77(2):573–580. https://doi.org/10.1007/s10064-017-1013-8
5. Zhan Y, Lu Z, Yao H, Xian S (2018) A coupled thermo-hydromechanical model of soil slope in seasonally frozen regions under freeze-thaw action. Adv Civil Eng. 2018(2018):1. https://doi.org/10.1155/2018/7219826
6. Filimonov MY, Kamnev YK, Shein AN, Vaganova NA (2022) Modeling the temperature field in frozen soil under buildings in the City of Salekhard taking into account temperature monitoring. Land 11(7):1102. https://doi.org/10.3390/land11071102
7. Plotnikov AA, Merzlyakov VP (2021) Increasing the bearing capacity and durability of building foundations on frozen soils. Soil Mech Found Eng 58(1):71–77. https://doi.org/10.1007/s11204-021-09708-0
8. Suter L, Streletskiy D, Shiklomanov N (2019) Assessment of the cost of climate change impacts on critical infrastructure in the circumpolar Arctic. Polar Geogr 42(4):267–286. https://doi.org/10.1080/1088937X.2019.1686082
9. Maadani O, Shafiee M, Egorov I (2021) Climate change challenges for flexible pavement in Canada: an overview. J Cold Reg Eng 35(4):1–8. https://doi.org/10.1061/(asce)cr.1943-5495.0000262
10. Song Y, Jin L, Peng H, Liu H (2020) Development of thermal and deformation stability of Qinghai-Tibet Highway under sunny-shady slope effect in southern Tanglha region in recent decade. Soils Found 60(2):342–355. https://doi.org/10.1016/j.sandf.2020.01.012
11. Tai B, Wu Q, Zhang Z, Xu X (2020) Study on thermal performance of novel asymmetric crushed-rock-based embankment on the Qinghai-Tibet Railway in permafrost region. Int J Therm Sci 152:106333. https://doi.org/10.1016/j.ijthermalsci.2020.106333
12. Dong S, Jiang Y, Yu X (2022) A novel random finite element model for holistically modeling of the frost effects on soils and cold region pavements. JIPR 3(1):16. https://doi.org/10.1186/s43065-022-00060-7
13. Qiao Y, Dawson AR, Parry T, Flintsch G, Wang W (2020) Flexible pavements and climate change: a comprehensive review and implicatio. Sustainability (Switzerland) 12(3):1–21. https://doi.org/10.3390/su12031057
14. Ud Din IM, Mir MS, Farooq MA (2020) Effect of freeze-thaw cycles on the properties of asphalt pavements in cold regions: a review. Transp Res Procedia 48:3634–3641. https://doi.org/10.1016/j.trpro.2020.08.087
15. Wu Y, Ishikawa T, Maruyama K, Ueno C, Yasuoka T, Okuda S (2022) Modeling wicking fabric inhibition effect on frost heave. Appl Sci 12(9):4357. https://doi.org/10.3390/app12094357
16. Zhuo Z, Ali A, Zhu C, Mehta Y, Lein W, DeCarlo C, Elshaer M, Kennedy D (2022) Evaluating the potential of using foamed concrete as the insulation layer for pavements in cold regions. Constr Build Mater 341:127903. https://doi.org/10.1016/j.conbuildmat.2022.127903
17. He R, Jin H (2010) Permafrost and cold-region environmental problems of the oil product pipeline from Golmud to Lhasa on the Qinghai-Tibet Plateau and their mitigation. Cold Reg Sci Technol 64(3):279–288. https://doi.org/10.1016/j.coldregions.2010.01.003
18. Li H, Lai Y, Wang L, Yang X, Jiang N, Li L, Wang C, Yang B (2019) Review of the state of the art: interactions between a buried pipeline and frozen soil. Cold Reg Sci Technol 157:171–186. https://doi.org/10.1016/j.coldregions.2018.10.014
19. Li X, Wu Q, Jin H (2022) Mitigation strategies and measures for frost heave hazards of chilled gas pipeline in permafrost regions: a review. Transp Geotech 36:100786. https://doi.org/10.1016/j.trgeo.2022.100786
20. Oswell JM (2011) Pipelines in permafrost: Geotechnical issues and lessons. Can Geotech J 48(9):1412–1431. https://doi.org/10.1139/t11-045
21. Liu Z, Yu X (2011) Coupled thermo-hydro-mechanical model for porous materials under frost action: theory and implementation. Acta Geotech 6(2):51–65. https://doi.org/10.1007/s11440-011-0135-6
22. Hansson K, Šimůnek J, Mizoguchi M, Lundin L, Genuchten MT (2004) Water flow and heat transport in frozen soil: numerical solution and freeze-thaw applications. Vadose Zone J 3(2):693–704. https://doi.org/10.2136/vzj2004.0693
23. Konrad JM (1994) Sixteenth Canadian geotechnical colloquium: frost heave in soils: concepts and engineering. Can Geotech J 31(2):223–245. https://doi.org/10.1139/t94-028
24. Noborio K, McInnes KJ, Heilman JL (1996) Two-dimensional model for water, heat, and solute transport in furrow-irrigated soil: II. Field evaluation. Soil Sci Soc Am J 60(4):1010–1021. https://doi.org/10.2136/sssaj1996.03615995006000040008x
25. Liu X, Rees SJ, Spitler JD (2007) Modeling snow melting on heated pavement surfaces. Part I: Model development. Appl Therm Eng 27(5–6):1115–1124. https://doi.org/10.1016/j.applthermaleng.2006.06.017
26. Tai B, Liu J, Wang T, Shen Y, Li X (2017) Numerical modelling of anti-frost heave measures of high-speed railway subgrade in cold regions. Cold Reg Sci Technol 141:28–35. https://doi.org/10.1016/j.coldregions.2017.05.009
27. Wang C, Ma Z (2021) Mathematical Model and Numerical Simulation of hydrothermal Coupling for Unsaturated Soil Subgrade in the Seasonal Frozen Zone. In: IOP Conference Series: Earth and Environmental Science. 719(3):1–8. https://doi.org/10.1088/1755-1315/719/3/032042

28. Xiao Z, Lai Y, Zhang J (2020) A thermodynamic model for calculating the unfrozen water content of frozen soil. Cold Reg Sci Technol 172:103011. https://doi.org/10.1016/j.coldregions.2020.103011
29. Amiri SAG, Grimstad G, Gao H, Kjelstrup S (2021) Numerical modelling of distinct ice lenses in frost heave. In: IOP Conference Series: Earth and Environmental Science, 710(1). https://doi.org/10.1088/1755-1315/710/1/012039
30. Bai R, Lai Y, You Z, Ren J (2020) Simulation of heat–water–mechanics process in a freezing soil under stepwise freezing. Permafrost Periglac Process 31(1):200–212. https://doi.org/10.1002/ppp.2028
31. Coussy O, Monteiro P (2007) Unsaturated poroelasticity for crystallization in pores. Comput Geotech 34(4):279–290. https://doi.org/10.1016/j.compgeo.2007.02.007
32. Li N, Chen B, Chen F, Xu X (2000) The coupled heat-moisture-mechanic model of the frozen soil. Cold Reg Sci Technol 31(3):199–205. https://doi.org/10.1016/S0165-232X(00)00013-6
33. Li Z, Chen J, Tang A, Sugimoto M (2021) A novel model of heat-water-air-stress coupling in unsaturated frozen soil. Int J Heat Mass Transfer 175:121375. https://doi.org/10.1016/j.ijheatmasstransfer.2021.121375
34. Sweidan AH, Niggemann K, Heider Y, Ziegler M, Markert B (2022) Experimental study and numerical modeling of the thermo-hydro-mechanical processes in soil freezing with different frost penetration directions. Acta Geotech 17(1):231–255. https://doi.org/10.1007/s11440-021-01191-z
35. Zheng H (2014) Study on a Practical Frost Heave Estimation With a Combined Thermal-Hydraulic and Mechanical Simulation. Hokkaido Univeristy, Hakkaido
36. Pi K, Bieroza M, Brouchkov A, Chen W, Dufour LJP, Gongalsky KB, Herrmann AM, Krab EJ, Landesman C, Laverman AM, Mazei N, Mazei Y, Öquist MG, Peichl M, Pozdniakov S, Rezanezhad F, Roose-Amsaleg C, Shatilovich A, Shi A, … Van Cappellen P (2021) The Cold Region Critical Zone in Transition: Responses to Climate Warming and Land Use Change. Annu Rev Environ Resour. 46:111–134. https://doi.org/10.1146/annurev-environ-012220-125703
37. Vardon PJ (2015) Climatic influence on geotechnical infrastructure: a review. Environmental Geotechnics 2(3):166–174. https://doi.org/10.1680/envgeo.13.00055
38. Cannon AJ, Jeong DIl, Zhang X, Zwiers FW (2020) Resilient buildings and core public infrastructure: an assessment of the impact of climate change on climatic design data in Canada. In Government of Canada, Gatineau
39. Duvillard PA, Ravanel L, Marcer M, Schoeneich P (2019) Recent evolution of damage to infrastructure on permafrost in the French Alps. Reg Environ Change 19(5):1281–1293. https://doi.org/10.1007/s10113-019-01465-z
40. Farquharson LM, Romanovsky VE, Cable WL, Walker DA, Kokelj SV, Nicolsky D (2019) Climate change drives widespread and rapid thermokarst development in very cold permafrost in the Canadian high arctic. Geophys Res Lett 46(12):6681–6689. https://doi.org/10.1029/2019GL082187
41. Hinzman LD, Bettez ND, Bolton WR, Chapin FS, Dyurgerov MB, Fastie CL, Griffith B, Hollister RD, Hope A, Huntington HP, Jensen AM, Jia GJ, Jorgenson T, Kane DL, Klein D R, Kofinas G, Lynch AH, Lloyd AH, McGuire AD, … Yoshikawa K (2005) Evidence and implications of recent climate change in Northern Alaska and other Arctic regions. Clim Change. 72(3):251–298. https://doi.org/10.1007/s10584-005-5352-2
42. Jorgenson MT, Racine CH, Walters JC, Osterkamp TE (2001) Permafrost degradation and ecological changes associated with a warming climate in central Alaska. Clim Change 48(4):551–579. https://doi.org/10.1023/A:1005667424292
43. Melvin AM, Larsen P, Boehlert B, Neumann JE, Chinowsky P, Espinet X, Martinich J, Baumann MS, Rennels L, Bothner A, Nicolsky DJ, Marchenko SS (2017) Climate change damages to Alaska public infrastructure and the economics of proactive adaptation. Proc Natl Acad Sci USA 114(2):E122–E131. https://doi.org/10.1073/pnas.1611056113
44. Mills BN, Tighe SL, Andrey J, Smith JT, Huen K (2009) Climate change implications for flexible pavement design and performance in Southern Canada. J Transp Eng 135(10):773–782. https://doi.org/10.1061/(ASCE)0733-947X(2009)135:10(773)
45. Rouse WR, Douglas MSV, Hecky RE, Hershey AE, Kling GW, Lesack L, Marsh P, Mcdonald M, Nicholson BJ, Roulet NT, Smol JP (1997) Effects of climate change on the freshwaters of arctic and subarctic North America. Hydrol Process 11(8):873–902. https://doi.org/10.1002/(SICI)1099-1085(19970630)11:8%3c873::AID-HYP510%3e3.0.CO;2-6
46. Streletskiy DA, Suter LJ, Shiklomanov NI, Porfiriev BN, Eliseev DO (2019) Assessment of climate change impacts on buildings, structures and infrastructure in the Russian regions on permafrost. Environ Res Lett 14(2):025003. https://doi.org/10.1088/1748-9326/aaf5e6
47. Larwa B (2019) Heat transfer model to predict temperature distribution in the ground. Energies 12(1):25. https://doi.org/10.3390/en12010025
48. Florides G, Kalogirou S (2007) Ground heat exchangers-A review of systems, models and applications. Renewable Energy 32(15):2461–2478. https://doi.org/10.1016/j.renene.2006.12.014
49. Zhang M, Wen Z, Xue K, Chen L, Li D (2016) A coupled model for liquid water, water vapor and heat transport of saturated–unsaturated soil in cold regions: model formulation and verification. Environ Earth Sci 75(8):1–19. https://doi.org/10.1007/s12665-016-5499-3
50. van Genuchten MTh (1980) A closed-form equation for predicting the hydraulic conductivity of unsaturated soils. Soil Sci Soc Am J 44:892–898
51. Koopmans RWR, Miller RD (1966) Soil Freezing and Soil Water Characteristic Curves. Soil Sci Soc Am J 30(6):680–685. https://doi.org/10.2136/sssaj1966.03615995003000060011x
52. Deng Q, Liu X, Zeng C, He X, Chen F, Zhang S (2021) A freezing-thawing damage characterization method for highway subgrade in seasonally frozen regions based on thermal-hydraulic-mechanical coupling model. Sensors 21(18):6251. https://doi.org/10.3390/s21186251
53. Tang T, Shen Y, Liu X, Zhang Z, Xu J, Zhang Z (2021) The effect of horizontal freezing on the characteristics of water migration and matric suction in unsaturated silt. Eng Geol. 288:106166. https://doi.org/10.1016/j.enggeo.2021.106166
54. Alavi MZ, Pouranian MR, Hajj EY (2014) Prediction of asphalt pavement temperature profile with finite control volume method. Transp Res Rec 2456(2456):96–106. https://doi.org/10.3141/2456-10
55. Huang K, Zollinger DG, Shi X, Sun P (2017) A developed method of analyzing temperature and moisture profiles in rigid pavement slabs. Constr Build Mater 151:782–788. https://doi.org/10.1016/j.conbuildmat.2017.06.120
56. Qin Y, Hiller JE (2013) Ways of formulating wind speed in heat convection significantly influencing pavement temperature prediction. Heat Mass Transfer/Waerme- Und Stoffuebertragung 49(5):745–752. https://doi.org/10.1007/s00231-013-1116-0
57. Xue J, Gavin K (2008) Effect of rainfall intensity on infiltration into partly saturated slopes. Geotech Geol Eng 26(2):199–209. https://doi.org/10.1007/s10706-007-9157-0
58. Dong S, Jiang Y, Yu X (2021) Analyses of the impacts of climate change and forest fire on cold region slopes stability by random finite element method. Landslides 18(7):2531–2545. https://doi.org/10.1007/s10346-021-01637-1

Publisher's Note